Kent Academic Repository

Downloaded from

The version of record is available from

This document version

Author's Accepted Manuscript

DOI for this version

Licence for this version

Additional information

Versions of research works

Versions of Record

If this version is the version of record, it is the same as the published version available on the publisher's web site. Cite as the published version.

Author Accepted Manuscripts

If this document is identified as the Author Accepted Manuscript it is the version after peer review but before type setting, copy editing or publisher branding. Cite as Surname, Initial. (Year) 'Title of article'. To be published in *Title of Journal* , Volume and issue numbers [peer-reviewed accepted version]. Available at: DOI or URL (Accessed: date).

Enquiries

Compact Dual-Polarized Continuous Transverse Stub Array With 2-D Beam Scanning

Tian Lou, Xue-Xia Yang, *Senior Member, IEEE*, Houtong Qiu, Zhangfei Yin, and Steven Gao, *Fellow, IEEE*

Abstract—A dual-polarized (DP) flat antenna array with passive 2-D beam-scanning capability is presented in this paper. The array consists of a DP continuous transverse stub (CTS) array, a flat Risley prism (FRP), and a line source generator. Two sets of CTSs, being constituted by the substrate-integrated waveguide (SIW), share a common aperture and are arranged orthogonally for the DP operation. A novel compact long line source is proposed for exciting this DP-CTS array. The FRP is realized by two linear phase progression phase-shifting surfaces (LPP-PSSs) and is placed above the DP-CTS array. The beam-scanning capability in the azimuth and in the elevation can be realized by rotating simultaneously the two LPP-PSSs in the same and in the opposite directions, respectively. A six-element array prototype is simulated and fabricated. According to the measured results, beam-scanning ranges of 40° in the elevation and 360° in the azimuth are achieved with the maximum gain of 17.8 dBi. The novel contributions from this paper include: 1) a novel compact long line source and 2) the first passive DP 2-D beam-scanning flat antenna array. This array can be extended easily to a higher gain or a circular polarization application.

Index Terms—Beam scanning, continuous transverse stub (CTS), dual polarization (DP), phase-shifting surface (PSS), substrate-integrated waveguide (SIW).

I. INTRODUCTION

WITH the advantages of saving power, high security, and decreasing interferences, beam-scanning antennas are required in many civilian and military applications. In a satellite communication (SatCom) on-the-move system, the beam-scanning array can guarantee the high-speed communication with high quality during the movement. Reflector antennas with mechanical control are a conventional solution [1], while they are bulky and require complicated mechanical control devices. Phased arrays have a flat profile and could steer beam fast; however, the phase shifters at every antenna

T. Lou, H. Qiu, and Z. Yin are with the School of Communication and Information Engineering, Shanghai University, Shanghai 200444, China (e-mail: loutian@shu.edu.cn; 810970463@qq.com; zf_yin1995@163.com).

X.-X. Yang is with the Key Laboratory of Specialty Fiber Optics and Optical Access Networks, Shanghai Institute for Advanced Communication and Data Science, Shanghai University, Shanghai 200444, China (e-mail: yang.xx@shu.edu.cn).

S. Gao is with the School of Engineering and Digital Arts, University of Kent, Canterbury CT2 7NZ, U.K. (e-mail: s.gao@kent.ac.uk).

element increase the complication and the cost of the antenna systems [2]–[4].

The continuous transverse stub (CTS) arrays were originally invented by Hughes Aircraft Company in the early 1990s [5]. The series-fed CTSs, being periodically arrayed on the parallel-plate waveguide, are fed by a linear source and act as the radiation elements with a leaky wave. The CTS array operates on the quasi-TEM mode of the parallel-plate waveguide, so it has good features of compact size, high gain, and low cross polarization [5]–[7]. Based on the coplanar waveguide feed structure, the ferroelectric phase shifters [6] and the metamaterial-based phase shifters [7] were employed to control the beam scanning of the CTS arrays. Recently, several passive CTS beam steering arrays have been proposed [8]–[12]. Ettorre *et al.* [8] designed a *Ka*-band CTS array with a scanning range of ±40° by moving a horn along a line. By using the substrate-integrated waveguide (SIW) technology, a flat frequency-scanned antenna with the scanning range of −16.8°–55.2° was designed in [9]. In [10], a CTS array fed by the ridged waveguide slot array had the scanning range of ±30° by rotating the whole feed structure. However, all aforementioned arrays operated on the linear polarization and could only achieve 1-D beam scanning. The variable inclination CTS (VICTS) antennas could scan in two directions; however, the scanning directions in the azimuth and the elevation are not independent and only operated on the linear polarization [11], [12].

With the rapid development of modern wireless communications, the spectrum becomes increasingly scarce, and the dual-polarization (DP) operation has been used to enhance the spectral efficiency and improve the channel capacity [13]. Several kinds of DP arrays have been proposed, such as the dipole [14], patch [15], [16], and the waveguide slot [17]. In recent publications, several CTS arrays are proposed for polarization diverse applications [18], [19]. However, these arrays had no beam-scanning function. Han *et al.* [20] proposed a *Ku*-band DP beam-scanning array by using hybrid phased-array technology. The array was bulky, complex, and expensive because many transmit/receive modules had been used. To the best of the authors' knowledge, no any 2-D passive beam-scanning DP flat array has been reported.

The phase-shifting surface (PSS) can control the transmission phase when the electromagnetic (EM) wave propagates through it, which has been used to design the planar microwave lens [21], [22], the near-field focusing antenna [23], and beam scanning antennas [24]–[26]. The 2-D beam-scanning antennas
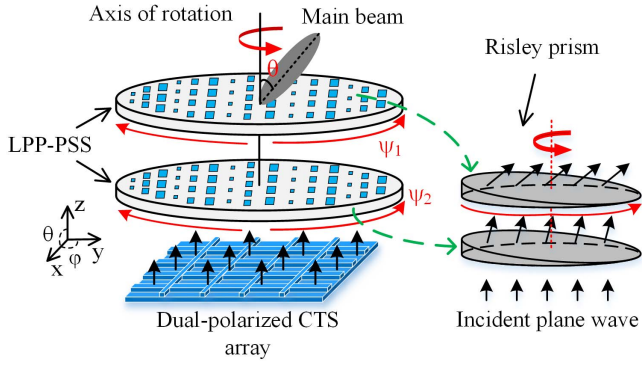
Fig. 1.   Principle of DP beam scanning (θ is in the xz plane and φ is in the xy plane).

Fig. 2.   Comparison of the PSS-based beam-scanning antennas. (a) Conventional. (b) Proposed.

were designed based on the principle of the Risley prism by using the PSS in [24] and [25]. In [24], a beam-scanning capability of 60° in elevation was achieved by combining two linear phase progression PSSs (LPP-PSSs) and a PSS planar lens together. In [25], a Fabry–Pérot cavity antenna was used as the active one to lower the profile of the antenna. However, the two antennas only operated on the linear polarization. A circularly polarized dual-band beam-scanning antenna fed by a horn was proposed in [26], and the beam-scanning ranges in elevation were from 0° to 50°. Inspired by the above literatures, in this paper, a passive DP flat antenna with 2-D beam-scanning capability will be presented for the first time by combining the DP-CTS array with the flat Risley prism (FRP).

Furthermore, in this paper, a novel line source generator (LSG) with compact size will also be proposed by using the SIW-based rectangular waveguide and the parabolic reflector based on our previous work in [27]. Two sets of LSG and long radiation stubs sharing the same aperture are arranged orthogonally for the DP radiation with high ports isolation and low cross polarization. By rotating the two LPP-PSSs above the DP-CTS array, 2-D beam scanning can be achieved. Compared with the PSS-based beam-scanning antennas in [24] and [26], this proposed array has a relatively low profile and compact size because the FRP is placed in the near-field region of the DP-CTS array. In addition, this array could be extended easily to meet a higher gain or a circular polarization application.

The rest of this paper is organized as follows. Section II presents the beam-scanning principle of this array. The analysis and the design of the FRP are addressed in Section III. Section IV describes the design and analysis of the LSG and the DP-CTS array. In Section V, we present the measurement and simulation results of our proposed antenna. Finally, conclusion is drawn in Section VI.

II. BEAM-SCANNING PRINCIPLE

Risley prism has been used for beam scanning in optics since the 1960s [28]. As shown in Fig. 1, the typical Risley prism consists of two-independent dielectric prisms that can rotate around the axis. When an incident plane wave propagating through the prisms, in turn, the propagation direction will be changed due to the refraction of the prisms. By controlling
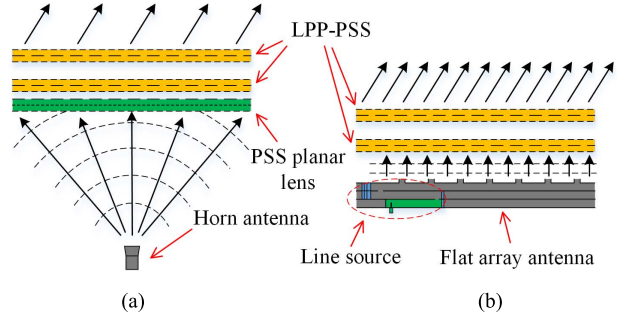
the relative rotation angle of the two prisms, the beam scanning can be achieved. The beam-scanning capability in the azimuth and in the elevation can be realized by rotating simultaneously the two dielectric prisms in the same and in the opposite directions, respectively.

At the microwave and millimeter-wave bands, dielectric prisms are bulky and lossy, which are not suitable for practical applications. In this paper, the dielectric prisms are replaced by two LPP-PSSs to reduce the volume of the Risley prism as shown in Fig. 1. The LPP-PSS consists of periodically arranged PSS elements with different transmission phase responses. Same as the dielectric prism, the beam direction of the plane wave will be tilted when it passes through the LPP-PSS. In this paper, by combining the LPP-PSS and the flat DP-CTS array, a 2-D beam scanning with DP is achieved. Two rotatable LPP-PSSs form an FRP, which are stacked upon the DP flat CTS array. The element of the PSS has the characteristic of polarization insensitive so the beam of two polarizations has the same direction. The DP beam can scan in both azimuth and elevation by rotating the two LPP-PSSs along the same or opposite direction.

Assuming the two LPP-PSSs having the same initial angles and rotating along the same direction, the rotation angles are denoted by Ψ_1 and Ψ_2, respectively. The rotation angles Ψ_1 and Ψ_2 vary between $-270°$ and $270°$, but $|\Psi_1 - \Psi_2|$ could not large than 180°. The azimuth angle of the beam, denoted as φ, is given as

$$\varphi = \frac{\psi_1 + \psi_2}{2}. \tag{1}$$

Accordingly, the rotation angles can be defined by φ as

$$\psi_1 = \varphi - \frac{\xi}{2} \tag{2a}$$

$$\psi_2 = \varphi + \frac{\xi}{2} \tag{2b}$$

where ξ is the relative rotation angle of the two LPP-PSSs. Assuming the beam tilt angle generated by an independent LPP-PSS is γ, referring to [25], the elevation angle θ of the beam is given as

$$\theta = 2\gamma \cos\frac{\xi}{2}. \tag{3}$$

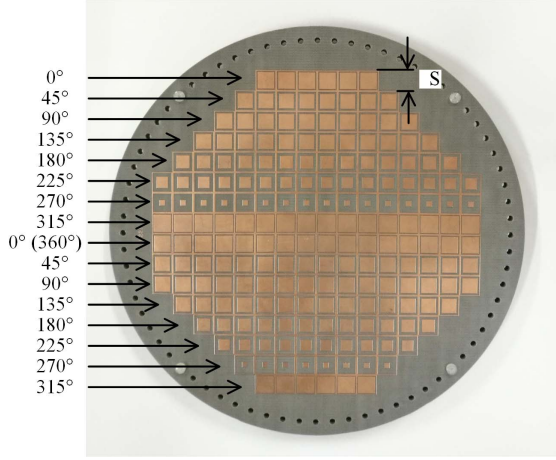The proposed beam-scanning array has the advantages of low profile and easy of extension. As shown in Fig. 2(a),

Fig. 3. Photograph of the proposed FRP.

Fig. 4. Configuration of the PSS cell.

TABLE I
DIMENSIONS AND THE PHASE SHIFT OF THE PSS CELLS

Cell number	Phase Shift (deg)	P_W₁ (mm)	P_W₂ (mm)	P_W₃ (mm)	P_W₄ (mm)	P_L₁ (mm)	P_L₂ (mm)	P_L₃ (mm)	P_L₄ (mm)
Cell 1	0	0.35	0.35	0.2	0.25	5.8	5.8	6.4	6.2
Cell 2	45	0.35	0.35	0.2	0.25	5.2	6	6.4	5.6
Cell 3	90	0.3	0.3	0.3	0.3	5.4	5.8	5.8	5
Cell 4	135	0.35	0.35	0.3	0.35	5.2	5.2	4.8	5
Cell 5	180	0.35	0.35	0.3	0.35	4.6	4.4	4.4	4.6
Cell 6	225	0.35	0.35	0.3	0.35	4	4	3.6	4
Cell 7	270	0.4	0.3	0.4	0.45	2	4	4	2
Cell 8	315	0.25	0.25	0.2	0.25	6.2	6.2	6.4	6.2

the conventional PSS-based beam-scanning antenna usually used a horn as a primary feed [24]. In order to increase the gain, the primary horn was placed at the focal point of the PSS planar lens to excite a plane wave. Therefore, the profile of the antenna is high. In our design, the LPP-PSSs are placed just above the flat CTS array as shown in Fig. 2(b). The flat CTS array radiates a quasi-plane wave at the near-field region so the PSS could be stacked close to the flat array, which results in a low profile. However, if the distance between the two parts is too close, the strong coupling will reduce the performance of the antenna. Therefore, the distance between the two parts will be a balance choice.

It is worth noting that two long line sources with the orthogonal position are necessary in order to obtain high ports isolation and low cross polarization of the CTS array. Furthermore, this DP array is easy to realize the circular polarization operation by an extra 90° phase difference network and is easy to enlarge the aperture for the higher gain application without increasing the thickness of the antenna.

III. FLAT RISLEY PRISM DESIGN

Fig. 3 shows the photograph of the proposed FRP. The FRP consists of periodically arranged PSS cells whose transmission phase is linearly progressing. In order to ensure the same phase difference between the adjacent cells, the PSS cells should cover a transmission phase-shift range from 0° to 360°. Usually, more phase quantization orders will make the phase distribution on the antenna aperture more uniform, considering the manufacturing accuracy, 3-bit phase quantization is chosen here. The FRP has eight steps of phase shift, which means that the phase difference between adjacent cells is $\delta = 45°$.

The tilt angle of the beam generated by an independent LPP-PSS is given as

$$\gamma = \arcsin \frac{\delta \lambda_0}{2\pi S} \qquad (4)$$

where λ_0 is the wavelength in free space and S is the period of the PSS cell.

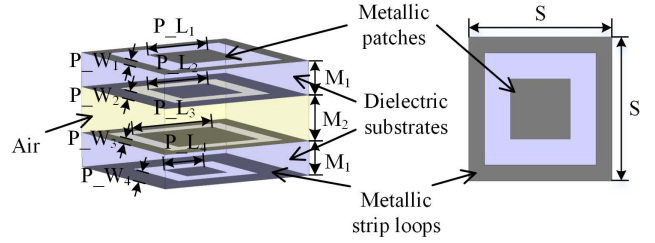As shown in Fig. 4, the PSS cell of one LPP-PSS includes four layers of the metal pattern, two layers of dielectric

substrate and an air layer. Each layer of the metal pattern consists of a metallic strip loop and a metallic patch, which are printed on the dielectric substrates of F4B with $\varepsilon_r = 2.65$, $\tan \sigma = 0.001$, and $M_1 = 1.5$ mm. An air layer is filled between the two dielectric substrates with the thickness of $M_2 = 2$ mm. This air layer is realized by using the polymethacrylimide foam layer. The period of this PSS cell is $S = 7.2$ mm. This cell could control the phase shift between the incident and transmitted waves while keeping the amplitude and the polarization almost unchanged. The shifted phase is determined by the widths of the metallic strip loops and the widths of the metallic patches on the four layers. This unit cell has a centrally symmetric structure, which results in isotropic characteristic.

Table I lists the dimensions of the PSS cells corresponding to different phase shifts (the phase shift of Cell 1 is the reference phase of 0°). The simulated transmission coefficients and phase-shift responses of the designed cells versus the frequency are shown in Fig. 5. From 12.25 to 12.68 GHz (3.4%), the transmission coefficients of all PSS cells are higher than −1.5 dB. Within the phase-shift range from 0° to 360°, the maximum phase error of the PSS cells is 9°.

In order to illustrate the impact of incident angle on the PSS cell performance, the transmission coefficient of Cell 1 and the transmission phase difference between the Cell 1 and Cell 2 at different incident angles are shown in Fig. 6. It can be seen from Fig. 6(a) that in the incident angle range of 30°, the variation of the transmission coefficient is less than 1 dB at the operation frequency of 12.5 GHz. As can be seen from Fig. 6(b), in the incident angle range of 30°, the variation
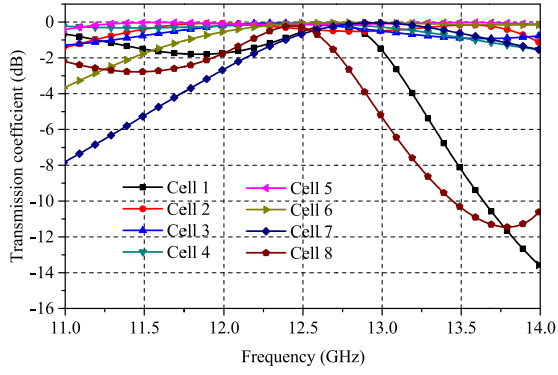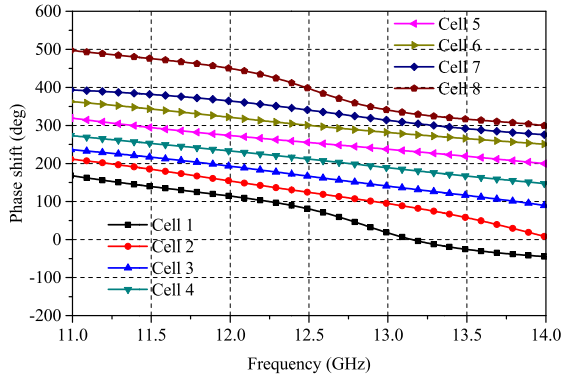
Fig. 5. (a) Transmission coefficients and (b) phase shifts of the designed PSS cells.

Fig. 6. (a) Transmission coefficient of Cell 1. (b) Transmission phase difference between the Cell 1 and Cell 2 at different incident angles.

of the transmission phase difference between the Cell 1 and Cell 2 is less than 4° at the operation frequency of 12.5 GHz.
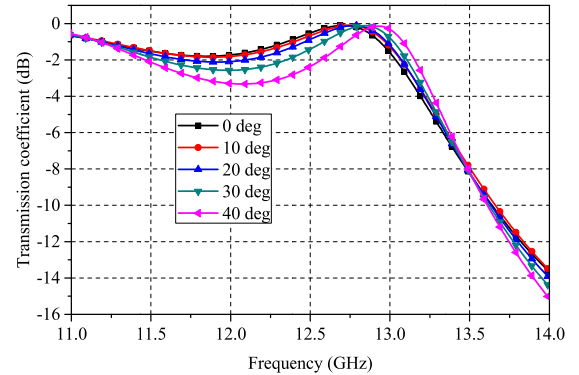
IV. DUAL-POLARIZED CTS ANTENNA DESIGN

Fig. 7 shows the exploded perspective view of the DP-CTS antenna array, which is stacked by four substrate layers. The substrates are also F4B. Sub 1 is the radiation layer, in which two SIW-CTSs are arranged orthogonally. The two SIW-CTS arrays radiate two orthogonally polarized quasi-plane waves. The feed structure is constituted by three substrate layers of Sub 2, Sub 3, and Sub 4. The thicknesses of Sub 1, Sub 2, Sub 3, and Sub 4 are H_1, H_2, H_3, and H_4, respectively.
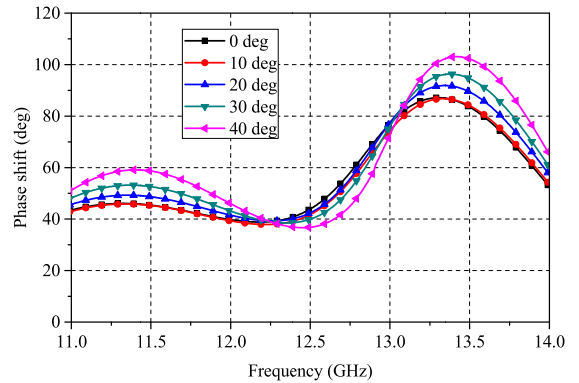
A. Compact LSG Design

The CTS array should be fed by an LSG that excites the plane wave. For feeding the DP-CTS array, a novel compact long line source is proposed. Fig. 8 shows the perspective, top, and side views of the proposed LSG. Based on the SIW technology, the LSG is composed of the coaxial-probe fed rectangular waveguide, the waveguide slot coupling structure, and the parabolic reflector coupling structure. The waveguide slot coupling structure is composed of the waveguide coupling slot and the metallic post reflector, while the parabolic reflector coupling structure is composed of the parabolic reflector and the parabolic coupling slot.

By placing the waveguide coupling slot at the focus of the parabolic reflector, a quasi-optical LSG would be achieved.

The producing process of the quasi-plane wave for the LSG could be explained as follows. First, the EM wave is excited by the coaxial probe and propagates along the SIW rectangular waveguide. Then, this EM wave is coupled from Sub 4 to Sub 3 by the slot etched on the upper surface of the waveguide, reflected by the metallic posts reflector, and form a quasi-cylindrical wave. Finally, this quasi-cylindrical wave would be transferred to a quasi-plane wave by the parabolic reflector coupling structure and coupled to Sub 2. The impedance matching of the whole LSG mainly depends on the structure parameters of W_1, W_2, W_3, and W_4.

This LSG is simulated by using the Ansoft High-Frequency Structure Simulator software. The amplitude and the phase characteristics along the transverse direction of the LSG [line A in Fig. 8(b)] are shown in Fig. 9. The amplitude distribution is approximately a cosine-cubed function, which is benefit from the operation mode of TE_{10} in the SIW rectangular waveguide. The maximum phase difference between the relative positions from 0.2 to 0.8 is less than 7°. Although the phase difference at the two far sides is high, it has little influence on the array performances because the electric field intensity is very low. Due to the amplitude distribution of the cosine-cubed function, low sidelobe levels (SLLs) in the H-plane would be achieved when the CTS array is fed by this LSG. Compared with the traditional standard pillbox system, the feed waveguide of the proposed LSG extends in the opposite direction, which is important in DP array design.
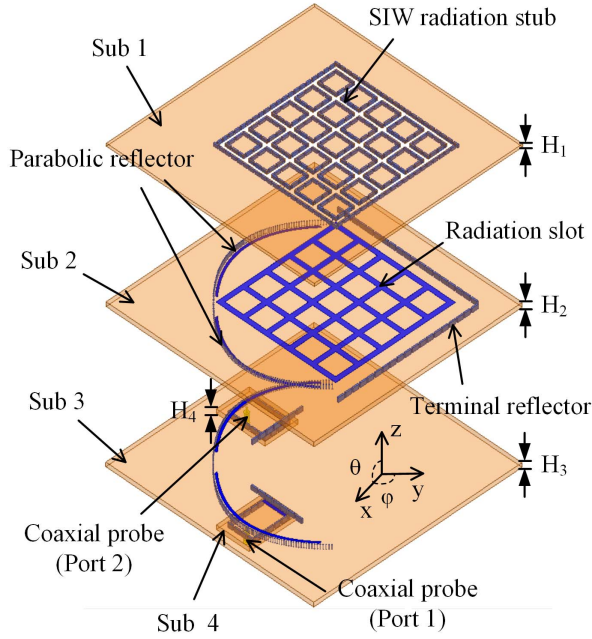
Fig. 7. Exploded perspective view of the DP-CTS antenna array (θ is in the xz plane and φ is in the xy plane).

Because the overlap of the feed waveguides could be avoided, especially when the array is small.

B. Dual-Polarized CTS Antenna Array

As shown in Fig. 7, two sets of long radiation stubs share a common aperture and are arranged orthogonally for the DP radiation. Two LSGs are placed orthogonally beside the CTS array to act as the feed structure, which is shown in Fig. 10. The quasi-plane wave excited by the LSG will be radiated from the radiation stubs. A finite 6×6 array is designed here. The radiation stubs spacing is about $0.64\lambda_0$ ($1.05\lambda_g$), where λ_0 and λ_g are the wavelengths in the free space and parallel-plate waveguide at 12.5 GHz, respectively. In order to radiate the energy as much as possible from the six radiation stubs, two-terminal reflectors are arranged behind the endmost radiation stubs of the orthogonal CTS array in Sub 2. The distance W_5 between the endmost radiation stub and the terminal reflector will affect the impedance match and the radiation performance of the antenna.

Fig. 11 shows the detailed sizes of the radiation layer. The radiation stubs are constructed by the metallic rectangular vias and rectangular long slots, which are etched on the upper and lower surfaces of Sub 1. The impedance matching is an important feature in antenna array design. The simulated reflection coefficients of the CTS array with different radiation stubs width W_6 and height H_1 are shown in Fig. 12. Due to the symmetry of the antenna structure, only the simulation results of port 1 are given. By optimizing these two parameters, the antenna can achieve a good impedance matching performance at the center operating frequency of 12.5 GHz. The distance L_6 between the radiation stubs and the permittivity of the substrate mainly affects the operation frequency of the
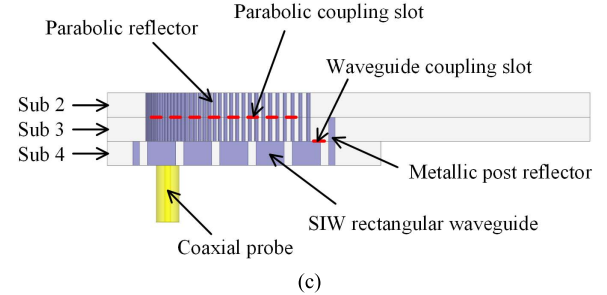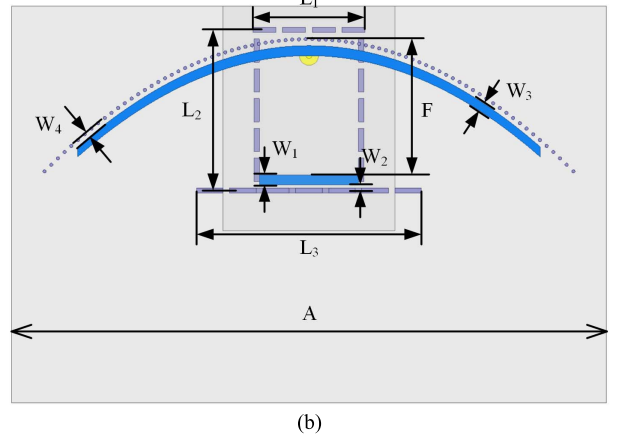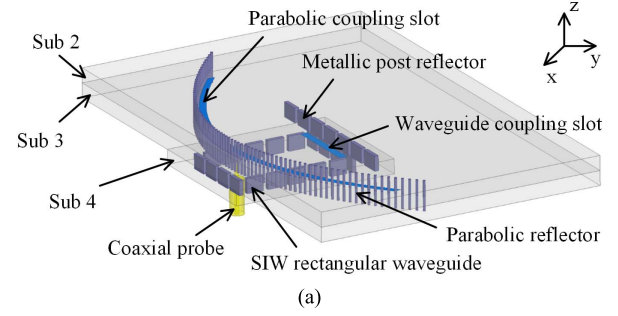

Fig. 8. Configuration of the LSG. (a) Perspective view. (b) Top view. (c) Side view.
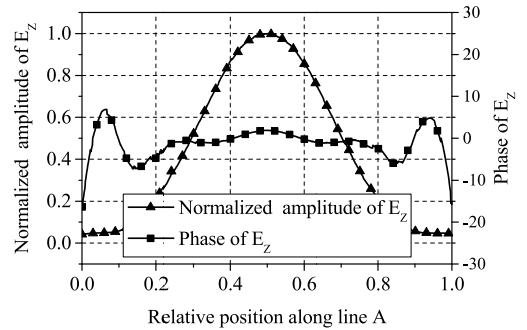

Fig. 9. Amplitude and the phase distributions of the electrical field along line A in Sub 2.

antenna. The simulated reflection coefficients with different ε_r and L_6 are plotted in Fig. 13. When ε_r and L_6 increase, the operating frequency decreases. It is worth mentioning that the parallel-plate waveguide mode of quasi-TEM in the CTS guarantees the high ports isolation and low cross-polarization performance of the antenna array. In addition, because the
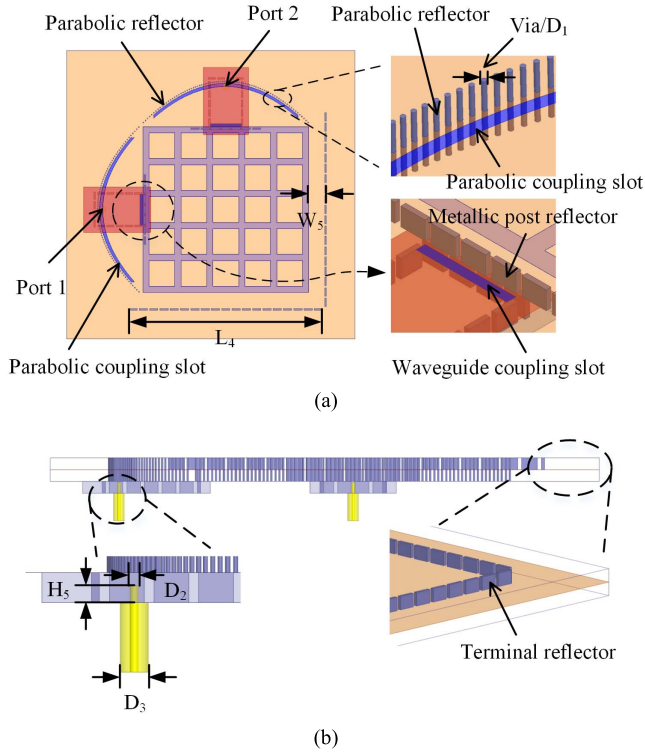
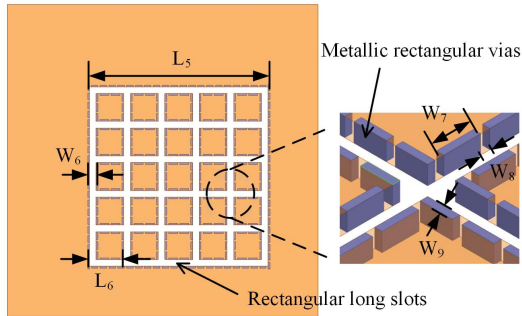Fig. 10. Feed structure of the DP-CTS antenna. (a) Top view. (b) Side view.

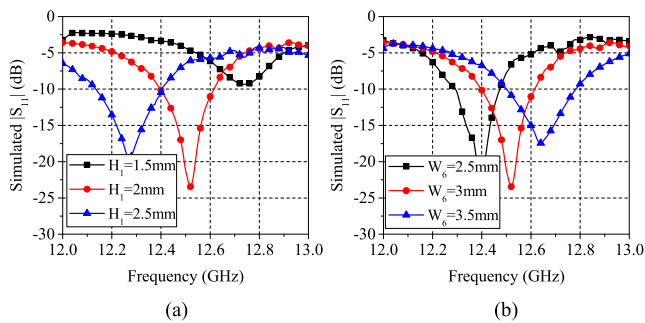Fig. 11. Geometrical sizes of the radiation layer.

Fig. 12. Simulated reflection coefficient with different (a) H_1 and (b) W_6.

transmission loss of parallel-plate waveguide is relatively small, the antenna has the potential to be designed in higher frequency applications.

C. Simulation Analysis of FRP Position

The FRP is placed in the near-field region of the DP-CTS array. Therefore, the interaction between the FRP and DP-CTS
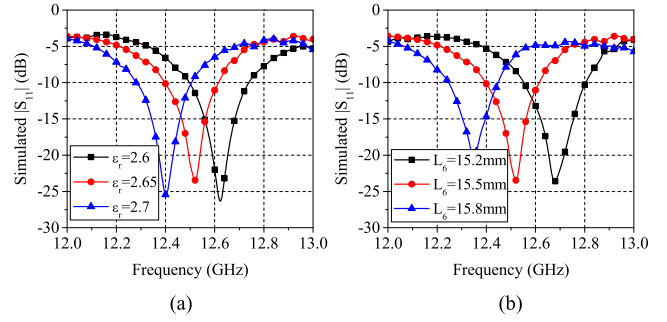

Fig. 13. Simulated reflection coefficient with different (a) ε_r and (b) L_6.
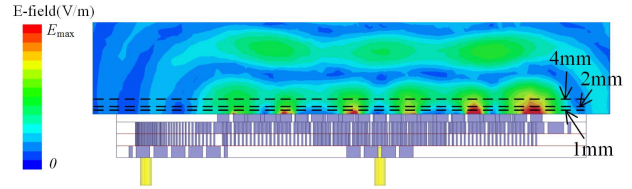

Fig. 14. Electrical field distributions of the DP-CTS array in the near-field region of the radiation aperture.
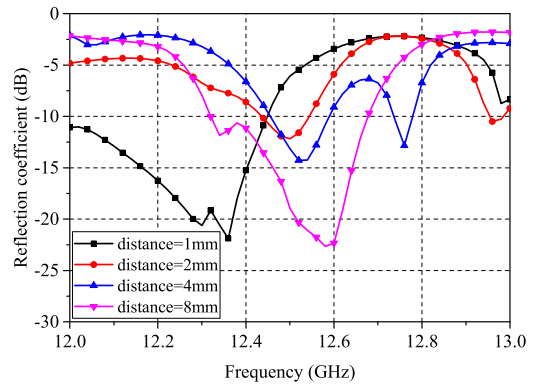

Fig. 15. Simulated reflection coefficients of the entire FRP + CTS antenna structure with different distances between the FRP and the CTS array.

array will affect the overall performance of the antenna. Fig. 14 shows the electrical field distribution of the DP-CTS array in the near-field region of the radiation aperture. Because each radiation stub can be regarded as an independent primary wave source, and there is space between the radiation stubs, the amplitude distribution of electric field near the antenna radiation aperture (1 mm above the antenna) is not uniform. The EM waves radiated by these radiation stubs continue propagating forward and superpose with each other. Because these radiation stubs radiate in phase, a quasi-plane wave with relatively uniform amplitude distribution is formed at a distance of about 4 mm from the antenna radiation aperture. Then, the quasi-plane wave will continue to propagate forward. Therefore, the FRP can be placed above this position to ensure that the electric field amplitude of the EM wave incident on each PSS cell is substantially equal.

In order to evaluate the effect of the coupling between FRP and DP-CTS array on the antenna performance, Fig. 15 shows the simulated reflection coefficient curves of the entire
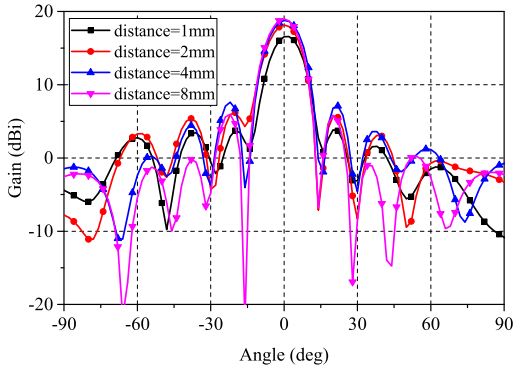
Fig. 16. Simulated radiation patterns of the entire FRP + CTS antenna structure with different distances between the FRP and the CTS array.

TABLE II
DIMENSIONS OF THE DP-CTS ARRAY (UNIT: MILLIMETER)

L_1	L_2	L_3	L_4	L_5	L_6	W_1	W_2	W_3
15	23.5	34	94	81.2	15.5	1.5	0.5	1.5
W_4	W_5	W_6	W_7	W_8	W_9	H_1	H_2	H_3
1	7	3	4	1	0.8	2	3	3
H_4	H_5	D_1	D_2	D_3	F			
3	2.7	0.5	0.87	2.9	21			

FRP + CTS antenna structure corresponding to different distances between the FRP and DP-CTS array when the antenna is set to broadside radiation. It can be seen that when the distance is too close, the reflection coefficient at the center operating frequency of 12.5 GHz increases significantly. Moreover, the −10 dB reflection coefficient band of the entire structure deviates from the operating band of the bottom DP-CTS. These differences are mainly caused by the coupling between FRP and CTS array. When the frequency deviates from 12.5 GHz, the transmission response of different PSS cells varies greatly. Due to different reflections at different locations of the FRP, new resonances may be generated. However, because both FRP and DP-CTS array operate in a narrow frequency band, only the influence of the distance between the two parts on the reflection coefficient near the center frequency needs to be considered. Fig. 16 shows the simulated radiation patterns corresponding to different distances when the antenna is set to broadside radiation at 12.5 GHz. When the distance is too close, the gain of the antenna decreases significantly. This is mainly caused by the coupling between the two parts and the nonuniform amplitude distribution of the electrical field on the radiation aperture of the bottom DP-CTS array. In general, the larger the distance between the FRP and the DP-CTS array, the smaller the coupling between them. However, this will increase the profile of the overall antenna. In addition, the excessive distance will let some EM waves leak from the edge of FRP, which will also reduce the antenna performance. Therefore, as a balance between the profile and the coupling, the distance is chosen to be 4 mm.

V. PROTOTYPE AND MEASUREMENTS

To validate the beam-scanning and DP performances of the proposed design, a 6 × 6 array prototype is fabricated and measured. Table II lists the main dimensions of the proposed
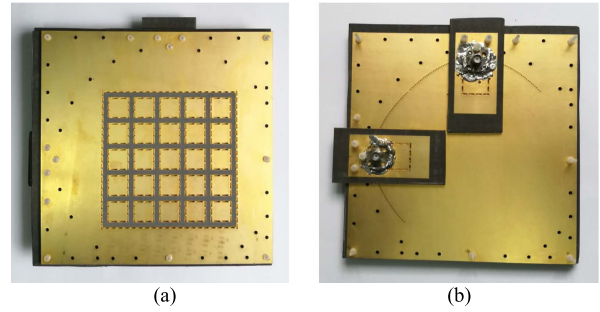

Fig. 17. Photographs of the DP-CTS antenna array. (a) Top view. (b) Bottom view.
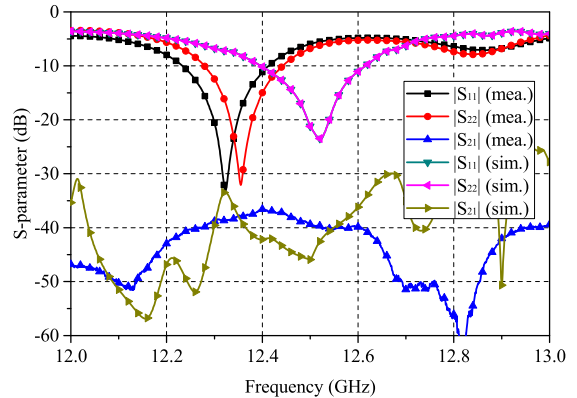

Fig. 18. Simulated and measured S-parameters versus frequency.

DP-CTS array. Fig. 17 shows the antenna photographs without the FRP. The height of the antenna is 11 mm ($0.46\lambda_0$).

As shown above, this beam-scanning antenna has two parts, the DP-CTS array on the low layer and the FRP for beam scanning on the upper one. The performances of the lower DP-CTS antenna and those of the whole assembled array antenna will be introduced in Sections V-A and V-B, respectively.

A. Dual-Polarized Operation Performances

The measured and simulated reflection coefficients and isolation versus the frequency are plotted in Fig. 18. According to the measured results, the −10 dB reflection coefficient bandwidth of ports 1 and 2 is from 12.24 to 12.41 GHz and from 12.28 to 12.44 GHz, respectively. Within this frequency range, the isolation between the two ports is higher than 35 dB. The measured operation frequency is a little lower than the simulated one. According to the analysis in Section IV-B, these discrepancies are mainly caused by the permittivity error of the dielectric substrate and the fabrication error. The proposed DP-CTS array is a series-fed resonant CTS standing wave array. Therefore, the operating bandwidth is relatively narrow. The operating bandwidth of this array is narrower than the designs of series-fed nonresonant CTS traveling wave array [9], [12] and corporate-fed CTS array [8], [10]. However, the proposed array has a similar bandwidth to the design of series-fed CTS standing wave array in [19].
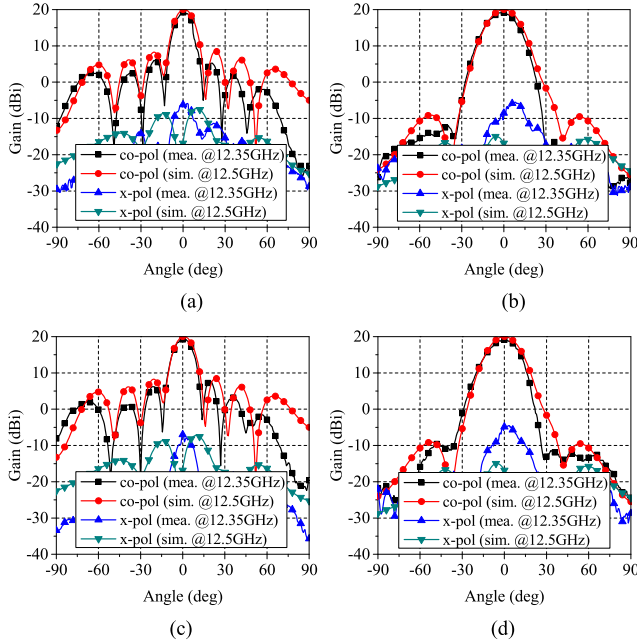
Fig. 19. Simulated and measured radiation patterns for ports 1 and 2. (a) E-plane for port 1. (b) H-plane for port 1. (c) E-plane for port 2. (d) H-plane for port 2.
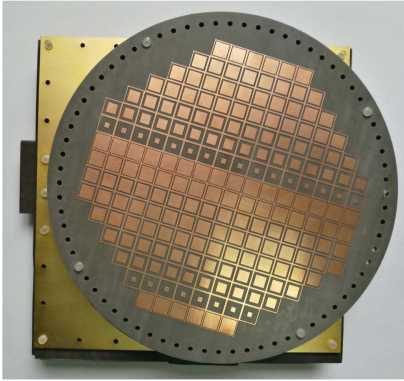

Fig. 20. Photograph of the assembled DP beam-scanning antenna array.

The measured and simulated radiation patterns of E- and H-planes for ports 1 and 2 are presented in Fig. 19, in which a good agreement could be found. For port 1, the measured gain at 12.35 GHz is 19.1 dBi with the maximum SLL in the E-plane of −13.3 dB and in the H-plane of −31.1 dB, respectively. The cross-polarization levels are lower than −22.3 dB in both planes. For port 2, the measured gain at 12.35 GHz is 19.2 dBi with the maximum SLL in the E-plane of −11.5 dB and in the H-plane of −28.5 dB, respectively. The cross-polarization levels are lower than −22.7 dB in both planes. It is observed that the antenna has a lower SLL in the H-plane, which benefits from the amplitude distribution of the plane wave generated by LSG being approximately a cosine-cubed function along the transverse direction (parallel to radiation stubs). The measured gains and cross-polarization discriminations deteriorate a little, which are mainly caused by the fabrication errors and assembly errors.

TABLE III
SCAN ANGLES COMPARISON BETWEEN THE THEORETICAL CALCULATION AND THE MEASUREMENT

ξ (deg)	180	155	130	100	65
Calculation (deg)	0	10.6	20.8	31.6	41.5
Measurement for port 1 (deg)	−3	6	16	25	34
Measurement for port 2 (deg)	4	12	17	30	43

TABLE IV
MEASURED GAIN VERSUS FREQUENCY

Frequency (GHz)	12.25	12.3	12.35	12.4	12.45
Gain (dBi)	15.7	16.1	16.2	16.4	16.1

B. Beam-Scanning Performances

By using the nylon screws, we assemble the FRP above the DP-CTS array for beam scanning. The assembled DP-CTS antenna array with the FRP is shown in Fig. 20. The overall height of the antenna is 28 mm ($1.17\lambda_0$). By rotating the two LPP-PSSs along the opposite direction with the same angle, the beam would scan in elevation.

Fig. 21 shows the simulated and measured radiation patterns of $\varphi = 0°$ plane for the beam scanning in elevation at 12.35 GHz for ports 1 and 2. The measured maximum gain and the maximum SLL for port 1 are 16.8 dBi and −6.7 dB, respectively. Those for port 2 are 17.8 dBi and −15.7 dB, respectively. When the LPP-PSSs rotate from 180° to 65°, the scan ranges for ports 1 and 2 are about 40° with the gain variation for port 1 of 1.7 dB and for port 2 of 3.0 dB. It also can be seen that the beams of the two polarizations are approximately in the same direction when the relative rotation angles of the LPP-PSSs are the same. The measured −3 dB beamwidths at broadside are 12.6° and 17.4° for ports 1 and 2, respectively. The variations of the −3 dB beamwidths for ports 1 and 2 are 2.6° and 7.6°, respectively. The difference results from the original bottom DP-CTS array have different patterns of E- and H-planes.

Table III shows the comparison of the scan angles calculated by (3) and (4) and the measurement. Although the maximum beam direction difference is 7.5° when ξ is 65°, the variation trend of calculation and measurement of the scan angles are consistent. It could be noted that the FRP is assumed to be excited by an ideal plane wave with uniform amplitude distribution and is fully transmitted in the calculation. However, in practical application, the characteristics of FRP and incident waves are not ideal. In addition, the manufacturing error and the manually setup process of the DP-CTS array and the FRP will also affect the measured scan angles.

Fig. 22 shows the simulated and measured cross-polarized level of the broadside and the maximum scanned angles for two ports. The cross-polarized level has been normalized to the corresponding copolarized ones. The measured and simulated cross-polarization levels are less than −17.9 and −23.9 dB, respectively. The deterioration is caused by the small amount
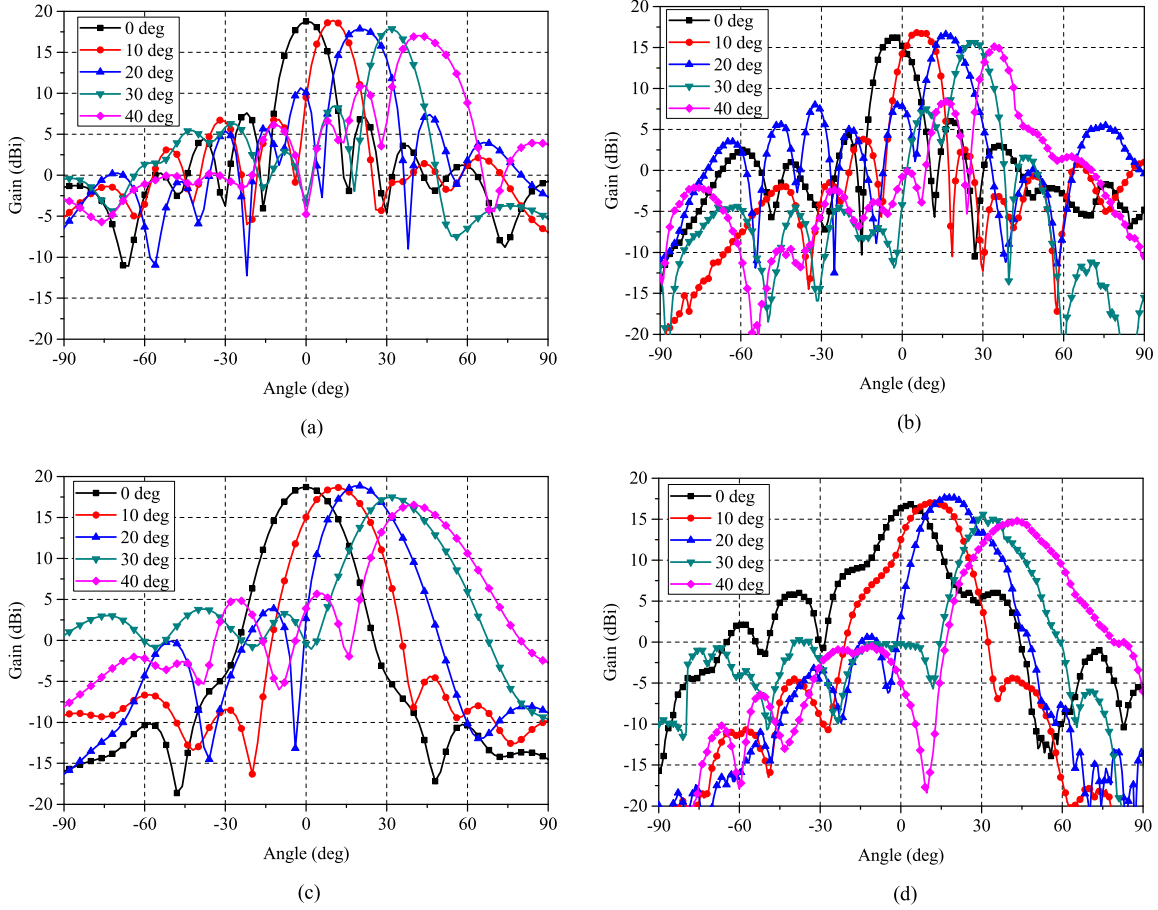
Fig. 21.   Simulated and measured radiation patterns of various elevation scan angles for port 1 and port 2 at 12.35 GHz (the scan angles of 0°, 10°, 20°, 30°, and 40° are corresponding to the relative rotation angle ξ of 180°, 155°, 130°, 100°, and 65°, respectively). (a) Simulated radiation patterns for port 1 ($\varphi = 0°$). (b) Measured radiation patterns for port 1 ($\varphi = 0°$). (c) Simulated radiation patterns for port 2 ($\varphi = 0°$). (d) Measured radiation patterns for port 2 ($\varphi = 0°$).
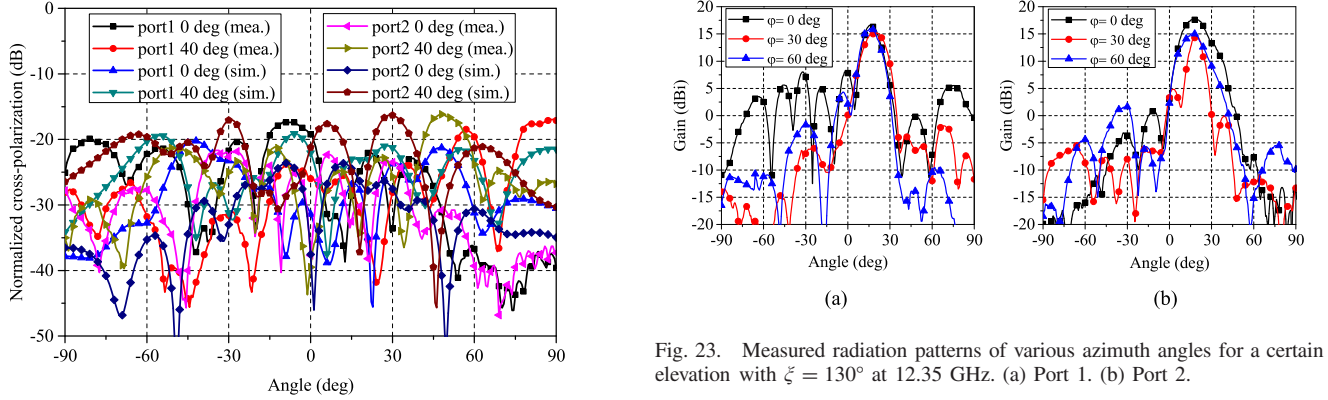

Fig. 22.   Simulated and measured normalized cross polarizations of broadside and maximum scanned beam for ports 1 and 2 at 12.35 GHz.

Fig. 23.   Measured radiation patterns of various azimuth angles for a certain elevation with $\xi = 130°$ at 12.35 GHz. (a) Port 1. (b) Port 2.

of EM energy coupled to the stubs that perpendicular to the plane wave. Table IV lists the measured gain versus frequency at the broadside. The maximum gain is 16.4 dBi at 12.4 GHz.

By rotating the two LPP-PSSs along the same direction with the same angle, the beam can scan in azimuth with the elevation angle unchanged. Fig. 23 shows the measured radiation

patterns at various azimuth angles when the elevation angle is 20° with the rotating angle ξ of 130°. The two polarizations have the same scan angle in elevation for different azimuth angles with the maximum gain variation of 3.3 dB. Because of the symmetry of the antenna structure, the proposed antenna is capable of scanning beams toward different directions to cover a full range of 360° in azimuth. Due to the limitation of the page, patterns at other azimuth and elevation angles are not presented here.

TABLE V

Refs.	[7]	[8]	[9]	[12]	[24]	[25]	[26]	This work
Polarization	Single linear	Single linear	Single linear	Single linear	Single linear	Single linear	Circular	Dual linear
Scanning angle range	58°~124°	±40°	−16.8°~55.2	±60°	±60° in elevation 360° in azimuth	±51° in elevation 360° in azimuth	±50° in elevation 360° in azimuth	±40° in elevation 360° in azimuth
Gain (dBi)	About 11.7	29	18.1	29.3	28	19.4	24 @ 20GHz 27 @ 30GHz	17.8
Aperture efficiency (%)	36.8	12.7	34.3	62	21.7	19.2	23.6 @ 20GHz 20.6 @ 30GHz	18.5
Dimension (L×W×H) (λ_0)	2×1.6×0.25	22.3×22.3×4.4	11.7×1.28×0.24	Not mentioned	15.2×15.2×8.3	6×6×1.27	9.2×9.2×8 @ 20GHz 13.9×13.9×12 @ 30GHz	5.1×5.1×1.17

Table V summaries the performances of the published beam-scanning antennas and our design. This paper has two novel contributions including: 1) a novel long line source with compact structure has been proposed and 2) a passive DP flat antenna with 2-D beam-scanning capability has been proposed for the first time by the combining of the DP-CTS array and FRP. Compared with the CTS beam-scanning antennas recently reported [6]–[12], our design has the advantages of DP radiation and 2-D beam scanning. Considering the full range of 360° scanning in azimuth, our design could cover a scan-angle range of ±40° in elevation, which is wider than most of previous CTS antenna designs. Although the VICTS antenna in [12] has a larger beam-scanning range, it can only operate on the linear polarization. Compared with the PSS-based beam-scanning antennas recently reported in [24] and [26], our design has the advantages of DP radiation and flat structure of low profile. Although the scan-angle range of several designs is wider than ours, the maximum gain variation criterions have been used such as 8.3 dB in [24], and 3.7 dB in [26], while ours is 3.3 dB. In addition, it is necessary to rotate the entire antenna to scan in azimuth in [26]. However, it just needs to rotate the FRP in our design, which will be more convenient. The design in [25] has a more similar profile compared to our design but it only operated on the linear polarization. Furthermore, our proposed SIW-CTS array is easy to enlarge the aperture for the higher gain application and to design the feed structure for the circular polarization operation.

VI. CONCLUSION

A passive DP 2-D beam-scanning CTS antenna array with a compact size is first presented in this paper. Another contribution is a novel LSG, which is easy to extend to feed large-size array or for circular polarization operation. The DP beam scanning in both the elevation and the azimuth directions is achieved by rotating the FRP above the DP-CTS antenna array in different directions. Benefiting from the compact-size feed structure that exciting the plane wave, the FRP could be put very close to the flat CTS array, so the profile of the antenna is reduced effectively. For the CTS array without FRP, the measured common −10 dB reflection coefficient bandwidth of the two ports is from 12.28 to 12.41 GHz with the isolation higher than 35 dB. The measured maximum gain is 19.2 dBi with the cross-polarization level being lower than −22.3 dB. The assembled antenna exhibits a beam-scanning capability of 40° in elevation and 360° in azimuth by rotating the two LPP-PSSs. In the scanning range, the maximum gains of the two ports are 16.8 and 17.8 dBi, respectively, while the maximum gain variations of the two ports are 1.7 and 3 dB, respectively. This DP 2-D beam-scanning antenna has a compact structure, a lightweight, and low cost, which has potential applications in the SatCom on-the-move systems.

REFERENCES

[1] W. L. Pritchard, "Satellite communication—An overview of the problems and programs," *Proc. IEEE*, vol. 65, no. 3, pp. 294–307, Mar. 1977.

[2] A. I. Zaghloul, O. Kilic, and E. C. Kohls, "System aspects and transmission impairments of active phased arrays for satellite communications," *IEEE Trans. Aerosp. Electron. Syst.*, vol. 43, no. 1, pp. 176–186, Jan. 2007.

[3] E. Topak, J. Hasch, C. Wagner, and T. Zwick, "A novel millimeter-wave dual-fed phased array for beam steering," *IEEE Trans. Microw. Theory Techn.*, vol. 61, no. 8, pp. 3140–3147, Aug. 2013.

[4] K. Y. Kapusuz, Ö. A. Civi, and A. G. Yarovoy, "A dual-band wide-angle scanning phased array antenna in K/Ka bands for satellite-on-the-move applications," in *Proc. 11th Eur. Conf. Antennas Propag. (EUCAP)*, Paris, France, Mar. 2017, pp. 1898–1902.

[5] W. W. Milroy, "Continuous transverse stub element devices and methods of making same," U.S. Patent 5 266 961 A, Nov. 30, 1993.

[6] W. Kim, M. F. Iskander, and W. D. Palmer, "An integrated phased array antenna design using ferroelectric materials and the continuous transverse stub technology," *IEEE Trans. Antennas Propag.*, vol. 54, no. 11, pp. 3095–3105, Nov. 2006.

[7] Y. Li, M. F. Iskander, Z. Zhang, and Z. Feng, "A new low cost leaky wave coplanar waveguide continuous transverse stub antenna array using metamaterial-based phase shifters for beam steering," *IEEE Trans. Antennas Propag.*, vol. 61, no. 7, pp. 3511–3518, Jul. 2013.

[8] M. Ettorre, F. F. Manzillo, M. Casaletti, R. Sauleau, L. Le Coq, and N. Capet, "Continuous transverse stub array for Ka-band applications," *IEEE Trans. Antennas Propag.*, vol. 63, no. 11, pp. 4792–4800, Nov. 2015.

[9] X.-X. Yang, L. Di, Y. Yu, and S. Gao, "Low-profile frequency-scanned antenna based on substrate integrated waveguide," *IEEE Trans. Antennas Propag.*, vol. 65, no. 4, pp. 2051–2056, Apr. 2017.

[10] X. Lu, S. Gu, X. Wang, H. Liu, and W. Lu, "Beam-scanning continuous transverse stub antenna fed by a ridged waveguide slot array," *IEEE Antennas Wireless Propag. Lett.*, vol. 16, pp. 1675–1678, 2017.

[11] W. W. Milroy, S. B. Coppedgen, and A. C. Lemons, "Variable inclination continuous transverse stub array," U.S. Patent 6 919 854 B2, Jul. 19, 2004.

[12] K. Tekkouk, J. Hirokawa, R. Sauleau, and M. Ando, "Wideband and large coverage continuous beam steering antenna in the 60-GHz band," *IEEE Trans. Antennas Propag.*, vol. 65, no. 9, pp. 4418–4426, Sep. 2017.

[13] J. J. A. Lempiainen and J. K. Laiho-Steffens, "The performance of polarization diversity schemes at a base station in small/micro cells at 1800 MHz," *IEEE Trans. Veh. Technol.*, vol. 47, no. 3, pp. 1087–1092, Aug. 1998.

[14] Y. Cui, R. Li, and H. Fu, "A broadband dual-polarized planar antenna for 2G/3G/LTE base stations," *IEEE Trans. Antennas Propag.*, vol. 62, no. 9, pp. 4836–4840, Sep. 2014.

[15] H. Wang, Y. Zhang, and W. Li, "Design of a dual-polarized patch array for millimeter-wave applications," in *Proc. IEEE Int. Conf. Ubiquitous Wireless Broadband (ICUWB)*, Nanjing, China, Oct. 2016, pp. 1–4.

[16] X. Zhao, B. N. Tian, S. P. Yeo, and L. C. Ong, "Low-profile broadband dual-polarized integrated patch subarray for X-band synthetic aperture radar payload on small satellite," *IEEE Antennas Wireless Propag. Lett.*, vol. 16, pp. 1735–1738, 2017.

[17] H. T. Zhang, W. Wang, M. P. Jin, Y.-Q. Zou, and X. Liang, "A novel dual-polarized waveguide array antenna for Ku band satellite communications," in *Proc. IEEE Int. Symp. Antennas Propag. USNC/URSI Nat. Radio Sci. Meeting*, San Diego, CA, USA, Jul. 2017, pp. 633–634.

[18] W. Milroy, "Inscribed polarizer array for polarization diverse application," U.S. Patent 9 941 594 B2, Apr. 10, 2018.

[19] Y. J. Cheng, J. Wang, and X. L. Liu, "94 GHz substrate integrated waveguide dual-circular-polarization shared-aperture parallel-plate long-slot array antenna with low sidelobe level," *IEEE Trans. Antennas Propag.*, vol. 65, no. 11, pp. 5855–5861, Nov. 2017.

[20] G. Han, B. Du, W. Wu, and B. Yang, "A novel hybrid phased array antenna for satellite communication on-the-move in Ku-band," *IEEE Trans. Antennas Propag.*, vol. 63, no. 4, pp. 1375–1383, Apr. 2015.

[21] M. A. Al-Joumayly and N. Behdad, "Wideband planar microwave lenses using sub-wavelength spatial phase shifters," *IEEE Trans. Antennas Propag.*, vol. 59, no. 12, pp. 4542–4552, Dec. 2011.

[22] A. H. Abdelrahman, A. Z. Elsherbeni, and F. Yang, "High-gain and broadband transmitarray antenna using triple-layer spiral dipole elements," *IEEE Antennas Wireless Propag. Lett.*, vol. 13, pp. 1288–1291, Jul. 2014.

[23] Y. C. Zhong and Y. J. Cheng, "Ka-band wideband large depth-of-field beam generation through a phase shifting surface antenna," *IEEE Trans. Antennas Propag.*, vol. 64, no. 12, pp. 5038–5045, Dec. 2016.

[24] N. Gagnon and A. Petosa, "Using rotatable planar phase shifting surfaces to steer a high-gain beam," *IEEE Trans. Antennas Propag.*, vol. 61, no. 6, pp. 3086–3092, Jun. 2013.

[25] M. U. Afzal and K. P. Esselle, "Steering the beam of medium-to-high gain antennas using near-field phase transformation," *IEEE Trans. Antennas. Propag.*, vol. 65, no. 4, pp. 1680–1690, Apr. 2017.

[26] S. A. Matos *et al.*, "High gain dual-band beam-steering transmit array for satcom terminals at Ka-band," *IEEE Trans. Antennas Propag.*, vol. 65, no. 7, pp. 3528–3539, Jul. 2017.

[27] T. Lou, X. Yang, L. Li, and E. Abubaker, "A flat dual-polarized continuous transverse stub antenna array based on substrate integrated waveguide," in *Proc. 12th Eur. Conf. Antennas Propag. (EuCAP)*, London, U.K., 2018, pp. 1–3.

[28] F. A. Rosell, "Prism Scanner," *J. Opt. Soc. Amer.*, vol. 50, no. 6, pp. 521–526, 1960.